Journal of Physics: Conference Series **3173** (2026) 012036 doi:10.1088/1742-6596/3173/1/012036

The Stability of The Frozen Top Bubble Model: Two-Dimensional Rayleigh-Bénard Convection on the Spherical Surface

Xiaoqiu HE[1,2,3], Patrick FISCHER[1], Khodor KHADRA[1], Yongliang XIONG[2,3]

[1]Institut de Mathématiques de Bordeaux, UMR 5251, Université de Bordeaux, Talence, France
[2]School of Aerospace Engineering, Huazhong University of Science and Technology Wuhan, China
[3]Hubei Key Laboratory of Engineering Structural Analysis and Safety Assessment, Huazhong University of Science and Technology, Wuhan, China

E-mail: xiaoqiuhe@hust.edu.cn

Abstract. Symmetry-breaking plays a fundamental role in fluid dynamics. We introduce the *frozen top bubble model*—a two-dimensional Rayleigh-Bénard convection (RBC) system on a spherical surface that features inherent vertical asymmetry between its hot and cold boundaries. A penalization method is used to impose a frozen, immobile, and cold region at the bubble's top, while heating is applied at the bubble's bottom, forming a convection cell with no lateral boundaries. Due to the bubble's geometry, the cold boundary is always shorter than the hot one, which significantly impacts the flow stability. When the asymmetry is strong, convection is suppressed, leading to a *stagnant regime* (SR) that becomes unstable as the Rayleigh number (Ra) increases. Conversely, reduced asymmetry results in an *active regime* (AR), where thermal convection remains robust regardless of Ra. These two regimes underscore the critical influence of vertical asymmetry on the stability of thermal convection.

1 Introduction

Thermal convection plays a vital role in geophysics, astrophysics, and engineering applications such as cooling systems [1, 2]. Rayleigh-Bénard convection (RBC) serves as a canonical model for understanding thermal convection and has been extensively studied. In its classical form, RBC consists of a fluid layer confined between two horizontal plates at constant temperatures, with the bottom plate being hotter than the top one.

The soap bubble model has recently emerged as a promising tool to investigate two-dimensional turbulence relevant to atmospheric dynamics [3]. In pioneering experiments, Kellay successfully maintained a hemispherical soap bubble on a platform for extended durations without

bursting [4]. By heating the bubble from below, complex flow phenomena emerged [5]. The ultra-thin soap film makes the system effectively two-dimensional, and the spherical geometry resembles planetary atmospheres [5]. Many large-scale atmospheric structures, such as cyclones, exhibit quasi-two-dimensional behavior due to their large horizontal-to-vertical aspect ratios [6]. Studying real atmospheric cyclones is both costly and challenging; thus, the soap bubble model provides a practical and insightful alternative [6, 7].

Both experiments [6, 7] and direct numerical simulations (DNS) [8, 9] have demonstrated the formation of large, long-lived vortices resembling atmospheric cyclones. Researchers have even developed predictive methods for their trajectories and their intensities, which have shown consistency with meteorological observations [6, 7]. Moreover, this model has been used to explore turbulence and thermal convection mechanisms. Using DNS, Bruneau et al. analyzed the scaling laws for Nusselt and Reynolds numbers and examined small-scale turbulence properties [9]. The model has since been extended to include rotating [10, 11] and tilted configurations [12], revealing inverse energy cascades and Bolgiano–Obukhov (BO59) scaling [9, 10]. Intermittency in both velocity and temperature fields has also been observed and analyzed [13].

However, in most DNS implementations of the soap bubble model, only a heating boundary is applied at the equator, with no corresponding cooling boundary at the top. This deviation limits its universality for studying thermal convection. To address this, we introduce the *frozen top bubble model*—a modified version of the soap bubble model that incorporates a cold, immobile zone at the top using a penalization method [14]. This model more closely resembles the classical RBC setup, with both heating and cooling mechanisms in place, while preserving the geometric advantages of the bubble.

Notably, this model introduces an intrinsic vertical asymmetry: the cold boundary is consistently shorter than the hot boundary. This vertical asymmetry plays a significant role in flow dynamics and stability. Although previous studies have explored the effects of symmetry breaking in RBC [15], lateral boundary conditions often complicate the analysis. The frozen top bubble model offers a unique opportunity to isolate and study the effects of vertical asymmetry without lateral interference. Furthermore, our model is an improvement on the previous model because it allows us to take into account the ice caps located on the poles. Indeed, on Earth, these polar zones are much colder and smaller than the equatorial zone.

The remainder of this paper is organized as follows: first, we present the model and numerical methods used in the simulations, followed by a discussion of the numerical results. Finally, we conclude with key findings and their implications.

2 Methodology

2.1 The Frozen Top Bubble Model

In our DNS simulations, the system consists of a hemispherical soap bubble of radius R placed on a horizontal plane. The bubble is modeled as a two-dimensional hemispherical surface, justified by two considerations: (i) the thickness of the soap film is negligible compared to the bubble's radius, and (ii) the bubble's weight is small enough that gravitational deformation is minimal.

The bubble features a single physical boundary—the equator (denoted as $\mathcal{L}_h$)—which is heated and subject to a no-slip condition. To introduce a cold boundary at the top, we impose a frozen region Ω_0 using a penalization method. The fluid is immobile and maintained at a uniform low temperature throughout the domain Ω_0. The remaining region, Ω_1, is the convection zone where active flow occurs. The interface between Ω_0 and Ω_1 acts as the cold boundary L_c, which is also no-slip and isothermal. As a result, Ω_1 effectively forms a Rayleigh-Bénard convection cell on a spherical surface.

The entire domain Ω is described in the spherical coordinates (r, θ, ϕ), where the radius

$r \equiv R$ is constant and thus eliminated from the governing equations. The polar angle $\theta \in [0, \pi/2]$ spans from the top of the bubble to the equator, and the azimuthal angle $\phi \in [0, 2\pi[$ spans the horizontal direction. The frozen zone corresponds to $0 \leq \theta \leq \theta_c$, and the convection zone to $\theta_c < \theta \leq \pi/2$. Figure 1(a) shows the geometry of Ω, including Ω_0 and Ω_1.

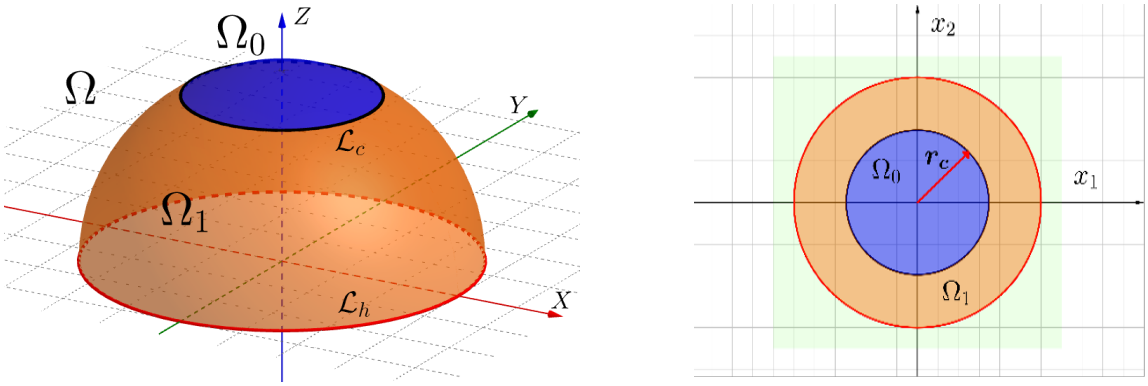

(a) View in 3D Cartesian coordinates (b) View in the projected coordinates

Figure 1: Geometry of the frozen top bubble. The blue part is the frozen zone (Ω_0) and the orange part is the convection zone (Ω_1). The black circle is the cold boundary ($\mathcal{L}_c$) and the red circle is the hot boundary ($\mathcal{L}_h$).

Within Ω_1, the flow is governed by the incompressible Navier–Stokes equations under the Boussinesq approximation. The system is non-dimensionalized using the bubble radius R, the temperature difference δT between the hot and cold boundaries, and the free-fall velocity $U_f = \sqrt{g\beta\delta T R}$, resulting in the following equations:

$$\nabla \cdot \mathbf{u} = 0 \tag{1}$$

$$\frac{\partial \mathbf{u}}{\partial t} + (\mathbf{u} \cdot \nabla)\mathbf{u} = -\nabla p + \sqrt{\frac{(\pi/2 - \theta_c)^3 \mathrm{Pr}}{\mathrm{Ra}}} \nabla^2 \mathbf{u} - T\mathbf{e}_g \tag{2}$$

$$\frac{\partial T}{\partial t} + (\mathbf{u} \cdot \nabla)T = \sqrt{\frac{(\pi/2 - \theta_c)^3 \mathrm{Pr}}{\mathrm{Ra}}} \nabla^2 T \tag{3}$$

where $\mathbf{u}$, p, T and $\mathbf{e}_g$ denote the non-dimensional velocity, the non-dimensional pressure, the non-dimensional temperature and the unit vector in the direction of gravity respectively. The Rayleigh and Prandtl numbers are defined as:

$$\mathrm{Ra} = \frac{g\beta\delta T H^3}{\nu\kappa}, \quad \mathrm{Pr} = \frac{\nu}{\kappa} \tag{4}$$

where ν is the kinematic viscosity, κ the thermal diffusivity, and $H = (\pi/2 - \theta_c)R$ is the vertical distance between the hot and cold boundaries. Although the system is non-dimensionalized using R, the Rayleigh number is defined based on H, since it characterizes the scale of thermal convection within Ω_1. Moreover, the aspect ratio W is defined as the ratio of the equator length to H:

$$W = \frac{2\pi R}{H} \tag{5}$$

It also indicates the relative surface area of Ω_1: as W increases, Ω_1 becomes smaller relative to Ω_0. The model exhibits vertical asymmetry as the cold boundary $\mathcal{L}_c$ is always shorter than the hot boundary $\mathcal{L}_h$. To quantify this asymmetry, we introduce a parameter A:

$$A = \frac{1}{\sin\theta_c} \tag{6}$$

where larger A corresponds to stronger asymmetry. A and W are uniquely related and cannot be adjusted independently. In summary, Ω_1 is bounded by the no-slip hot boundary L_h at $\theta = \pi/2$ with $T = 1$, and the cold boundary L_c at $\theta = \theta_c$ with $T = 0$. The initial conditions are $\mathbf{u} = 0$ and $T = 0$ inside Ω_1. The study mainly focuses on Ω_1, where convection dynamics are analyzed.

2.2 Numerical Methods

The non-dimensional governing equations (1)-(3) are solved within the stereographic coordinate system. After non-dimensionalization, the spherical coordinates (θ, ϕ) are transformed into non-dimensional Cartesian coordinates (x, y, z) via:

$$x = \cos\theta\cos\phi, \tag{7}$$

$$y = \cos\theta\sin\phi, \tag{8}$$

$$z = \sin\theta. \tag{9}$$

Then, the stereographic projection is applied to obtain the 2D coordinates (x_1, x_2):

$$x_1 = \frac{x}{1+z}, \tag{10}$$

$$x_2 = \frac{y}{1+z}. \tag{11}$$

In this coordinate system, the hemispherical bubble is projected onto a flat circular disk of unit radius. The computational domain is a square enclosing this disk, centered at the origin. The frozen zone Ω_0 is also mapped to a smaller disk with radius r_c given by:

$$r_c = \tan\frac{\theta_c}{2} \tag{12}$$

Figure 1 (b) illustrates the geometry and computational domain under stereographic projection. This approach effectively reduces one spatial dimension and simplifies numerical treatment by flattening the curved geometry.

The hot and cold boundaries of the convection zone Ω_1 are enforced using the penalization method [14]. In the numerical implementation of Equation (2), a penalization term $\frac{\boldsymbol{u}}{p_0^u}$ is added. The parameter p_0^u is set to 10^{16} inside Ω_1 (to freeze the velocity), and 10^{-16} elsewhere.

For the equation (3) describing the evolution of the temperature field T, two penalization terms are introduced: $\frac{T}{p_0^T}$ and $\frac{T-1}{p_1^T}$. The values are assigned as follows:

- $p_0^T = 10^{-16}$ inside Ω_0, and $p_0^T = 10^{16}$ outside Ω_0
- $p_1^T = 10^{-16}$ outside Ω_1 and $p_1^T = 10^{16}$ inside Ω_1

The numerical scheme is based on the finite difference method with time-splitting. Specifically, the energy equation (3) is solved using a biconjugate gradient method, while the coupled velocity-pressure equations (1) and (2) are solved using the Gauss–Seidel iterative method. Further implementation details can be found in [9, 10].

2.3 Configuration of the Parameters

In this study, the input parameters are the Rayleigh number Ra and the asymmetry parameter A, which is directly linked to the aspect ratio W. The Prandtl number is fixed at Pr = 7, corresponding to the physical properties of water, the primary constituent of the soap bubble. For each DNS run, we prescribe a fixed value of A and increase Ra progressively. A series of numerical simulations were performed, the input parameters corresponding to the results presented in this paper are summarized in Table 1.

Table 1: Summary of DNS parameters for different runs.

Run No.	Ra	θ_c (°)	Pr	A	W
1	1.12×10^4 – 1.12×10^{10}	1.1	7	50.01	4.05
2	7.74×10^3 – 7.74×10^9	11.4	7	5.05	4.58
3	2.89×10^3 – 2.89×10^9	33.4	7	1.82	6.36
4	7.99×10^2 – 7.99×10^9	53.1	7	1.25	9.76
5	3.49×10^3 – 3.49×10^9	84.0	7	1.01	59.75

3 Discussion

3.1 Stability Characteristics of the Frozen Top Bubble

The stability of the frozen top bubble system depends primarily on the asymmetry parameter A and the Rayleigh number Ra. In most simulations, the flow converged to a steady state, where physical quantities remained statistically stable. However, in certain cases, numerical divergence occurred after a large number of time steps. We define "numerical divergence" or "numerical blow-up" as the uncontrolled increase of the kinetic energy within the convective zone Ω_1. These observations suggest the existence of two distinct dynamical regimes.

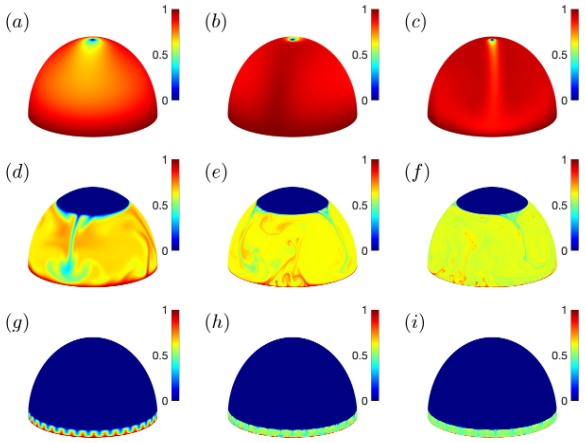

Figure 2: Snapshots of temperature in stationary state: (a)-(c) $A = 50.01$, $Ra = 1.12 \times 10^4$, 1.12×10^5 and 1.12×10^6; (d)-(f) $A = 1.82$, $Ra = 2.89 \times 10^6$, 2.89×10^8 and 2.89×10^9; (g)-(i) $A = 1.01$, $Ra = 3.49 \times 10^3$, 3.49×10^5 and 3.49×10^6.

To gain deeper insight into these two different regimes, Figure 2 shows snapshots of the temperature fields in stationary states for simulations that remain stable. The top row corresponds to $A = 50.01$ and Ra equal to 1.12×10^4, 1.12×10^5 and 1.12×10^6. The middle row

shows $A = 1.82$ with $Ra = 2.89 \times 10^6$, $Ra = 2.89 \times 10^8$ and $Ra = 2.89 \times 10^9$. The bottom row depicts $A = 1.01$ with $Ra = 3.49 \times 10^3$, 3.49×10^5, and 3.49×10^6. We can observe that for the simulations in the top row, thermal convection is very weak and the average temperature is very high. No turbulence can be observed. The increase of the Rayleigh number Ra fails to enhance thermal convection, and the flow loses its stability when Ra is greater than a certain value. Thus, this regime is named the Stagnant Regime (SR) since no turbulence can develop with these input parameters. For the simulations shown in the middle and bottom rows, thermal convection is active and becomes stronger with increasing Ra. More importantly, for this range of values of A, the flow remains stable for all tested values of Ra. Hence, we refer to this regime as the Active Regime (AR). The characteristics of two regimes are summarized below:

- **Stagnant Regime (SR)**: Thermal convection is constrained. The stability depends on Ra, and the flow tends to diverge at high Ra. This regime occurs for relatively large values of A.
- **Active Regime (AR)**: Thermal convection is active, and the flow remains stable across all tested values of Ra. This regime occurs for relatively small values of A (close to 1).

3.2 Divergence Induced by the Inverse Energy Cascade

To further investigate the origin of the numerical divergence, we analyze the total kinetic energy E_{Ω_1} in the convection zone Ω_1, defined as:

$$E_{\Omega_1} = \iint_{\Omega_1} \frac{1}{2}(\boldsymbol{u} \cdot \boldsymbol{u}) \mathrm{d}s \tag{13}$$

For the highly asymmetric case $A = 50.01$, Figure 3 shows the time evolution of E_{Ω_1} in the SR on a logarithmic scale. When Ra is relatively low, the kinetic energy is close to zero at the beginning, indicating the absence of convection due to the initial condition. As the simulation proceeds, E_{Ω_1} gradually increases and eventually reaches a plateau, reflecting convergence to a statistically steady state.

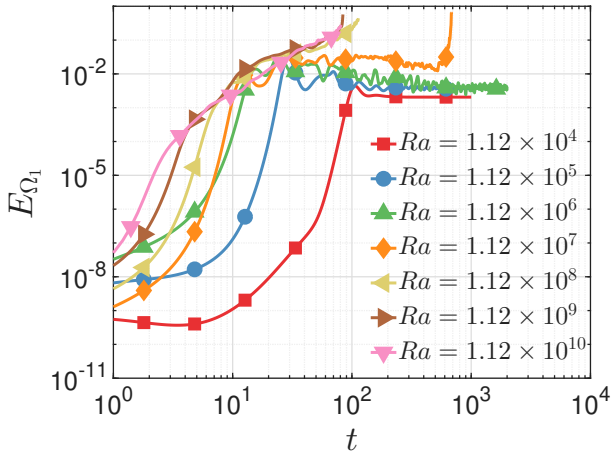

Figure 3: Temporal evolution of E_{Ω_1} for $A = 50.1$

However, at sufficiently high Rayleigh numbers (for instance from $Ra = 1.12 \times 10^7$ for $A = 50.1$), E_{Ω_1} begins to grow rapidly, eventually leading to a numerical blow-up in finite time. A similar trend is also observed for $A = 5.05$. This transition suggests that the flow becomes

unstable due to an enhanced inverse energy cascade. Figure 4 provides the snapshots of the local kinetic energy and the absolute value of vorticity fields for the case $Ra = 1.12 \times 10^{10}$ and $A = 50.01$ just before the numerical divergence. The vorticity fields show that the vortices are very strong and large indicating that the inverse energy cascade is the prime reason for the numerical blow-up. The numerical blow-up is observed even in regimes where thermal convection is effectively suppressed due to a globally uniform temperature field. Computational results reveal that small, weakly advecting vortical structures gradually aggregate and merge, forming a dominant large-scale vortex. This aggregation process is characterized by an extended period of quasi-steady development. Nonetheless, given a sufficiently long integration time, the principal vortex exhibits pronounced amplification and maintains a persistent acceleration in growth, ultimately precipitating divergence in the numerical solution.

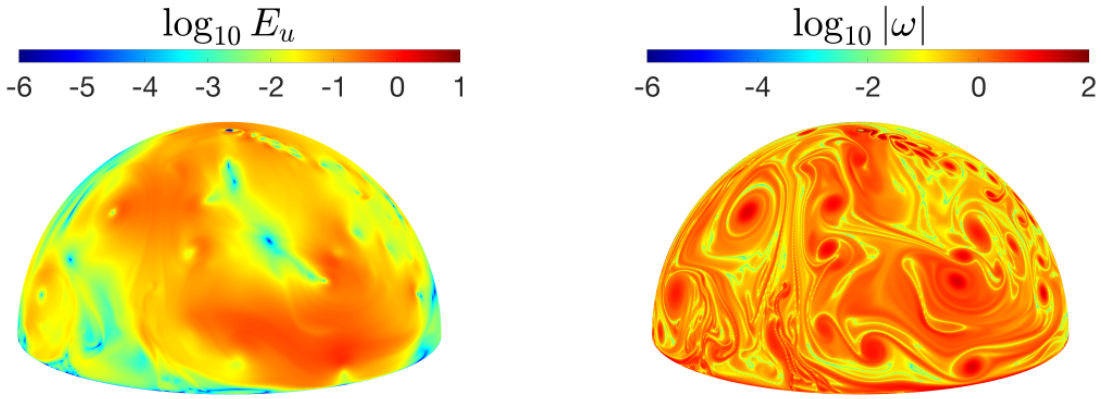

(a) Instantaneous kinetic energy (log scale) field for $Ra = 1.12 \times 10^{10}$ and $A = 50.01$

(b) Instantaneous vorticity magnitude (log scale) field for $Ra = 1.12 \times 10^{10}$ and $A = 50.01$

Figure 4: Kinetic energy and vorticity fields showing the inverse energy cascade.

In the direct numerical simulations of the original bubble model (two-dimensional thermal convection under the Boussinesq approximation without any extra dissipative terms in the equations), the authors observed flow fields similar to those in Figure 4 [8, 9, 10]. As a result, the authors had to introduce a friction term for the velocity (and also a thermal dissipation term) into the mathematical model of the bubble, in order to suppress the instability caused by the inverse energy cascade [9, 10]. This is a common practice in DNS of two-dimensional turbulence [16]. However, the friction term is deliberately omitted in this study of the frozen top bubble model to stay as close as possible to the classical Rayleigh-Bénard framework. As the parameter A increases, the frozen top bubble model tends to the original bubble model without the extra friction term. Therefore, the observed divergence can be explained by the inverse energy cascade and the accumulation of energy at the largest scale implied by the size of the bubble.

3.3 Quantitative Difference Between Two Regimes

To further explore the differences between the two regimes described above, we define the global average temperature T_{Ω_1} as,

$$T_{\Omega_1} = \frac{\oiint_{\Omega_1} T \mathrm{d}s}{\oiint_{\Omega_1} 1 \mathrm{d}s}. \tag{14}$$

The Ra-A phase space displayed in Figure 5(a) allows us to describe the stability behavior of the system as a function of A and Ra. The results indicate that for strongly asymmetric cases

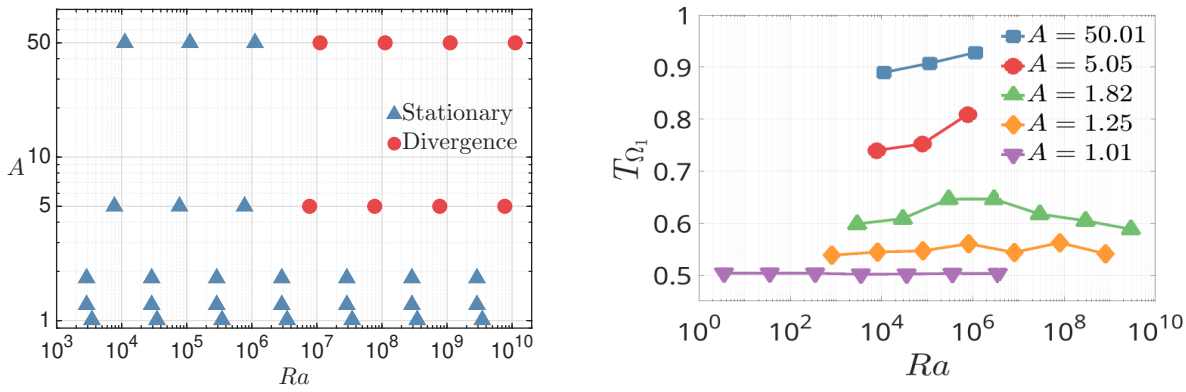

(a) Stability of the DNS as a function of A and Ra

(b) Variation of T_{Ω_1} as a function of Ra and A.

Figure 5: Differences between the active state and the stagnant state: stability states and variation patterns of T_{Ω_1}

($A \geq 5$), numerical divergence occurs as Ra increases. In contrast, when asymmetry is weak ($A \leq 1.82$), the simulations remain stable regardless of the Rayleigh number.

Figure 5 (b) shows T_{Ω_1} as a function of Ra for different values of A. The results clearly distinguish the behaviors of the SR and AR regimes. In the SR, the average temperature T_{Ω_1} is significantly higher than in the AR, and it increases monotonically with increasing A, suggesting that the temperature is globally higher when the cold boundary becomes shorter. The global average temperature is determined by the balance between the non-dimensional heat flux H_{in} produced at $\mathcal{L}_h$ and defined by,

$$H_{in} = \oint_{\mathcal{L}_h} \frac{\partial T}{\partial \theta} \mathrm{d}s = \int_0^{2\pi} \frac{\partial T}{\partial \theta} \mathrm{d}\phi \tag{15}$$

and the non-dimensional heat flux H_{out} absorbed at $\mathcal{L}_c$ defined by:

$$H_{in} = \oint_{\mathcal{L}_c} \frac{\partial T}{\partial \theta} \mathrm{d}s = \int_0^{2\pi} \cos\theta_c \frac{\partial T}{\partial \theta} \mathrm{d}\phi \tag{16}$$

For a given temperature gradient $\dfrac{\partial T}{\partial \theta}$, H_{in} is always greater than H_{out} for two reasons: (i) the length of $\mathcal{L}_h$ is always larger than the length of $\mathcal{L}_c$; (ii) the projection of the gravitational force on $\mathcal{L}_h$ is also greater than the projection on $\mathcal{L}_c$. In the stationary state, T_{Ω_1} increases sufficiently to reduce the temperature gradient at $\mathcal{L}_h$ and increase it at $\mathcal{L}_c$. Therefore, H_{in} decreases and H_{out} increases, reaching an equilibrium. As A increases, the gravitational component projected along $\mathcal{L}c$ diminishes, concurrently shortening the length of $\mathcal{L}c$. Consequently, T_{Ω_1} increases to maintain equilibrium.On the other hand, T_{Ω_1} increases monotonically with increasing Ra in the SR.

In the AR, T_{Ω_1} exhibits non-monotonic behavior as Ra increases. For relatively large values of A, such as 1.85, T_{Ω_1} initially increases with Ra but later decreases. When A approaches 1, T_{Ω_1} remains constant.

The results in Figure 2 highlight a distinct contrast between the SR and the AR. In the SR (top row), thermal convection remains inactive even as Ra increases. Due to the strong asymmetry, $\mathcal{L}_c$ is much shorter than $\mathcal{L}_h$ and is also located very close to the top, leading to a weak projected gravitational component. Consequently, thermal convection near $\mathcal{L}_c$ is heavily

suppressed, obstructing heat transport out of the convective zone. In the process of reaching the stationary state, the heat injected from $\mathcal{L}_h$ accumulates inside the convection zone, pushing T_{Ω_1} to high values. The elevated T_{Ω_1} balances H_{in} and H_{out} by significantly weakening thermal convection near $\mathcal{L}_h$. As Ra increases, H_{in} is initially enhanced then suppressed by the rise in T_{Ω_1}. However, H_{in} remains constrained due to the dominant asymmetry. Therefore, a higher T_{Ω_1} is required to balance the $H_{\text{out}}/H_{\text{in}}$ ratio.

For the AR, Figure 2 shows that thermal convection is active and strengthens with increasing Ra. As the parameter A tends to 1 (bottom row), the cold boundary $\mathcal{L}_c$ moves away from the top of the bubble. The projected component of the gravitational force near $\mathcal{L}_c$ increases enhancing thermal convection near $\mathcal{L}_c$. Moreover, the length of $\mathcal{L}_c$ increases, allowing stronger heat transport out of the convection zone. In the AR, heat crosses the convection zone instead of accumulating within it. The moderate T_{Ω_1} has the capacity to balance H_{in} and H_{out}. In addition, H_{in} and H_{out} are both enhanced since the effect of asymmetry is less significant. Hence, a large value of T_{Ω_1} is not required to balance H_{in} and H_{out} when Ra increases.

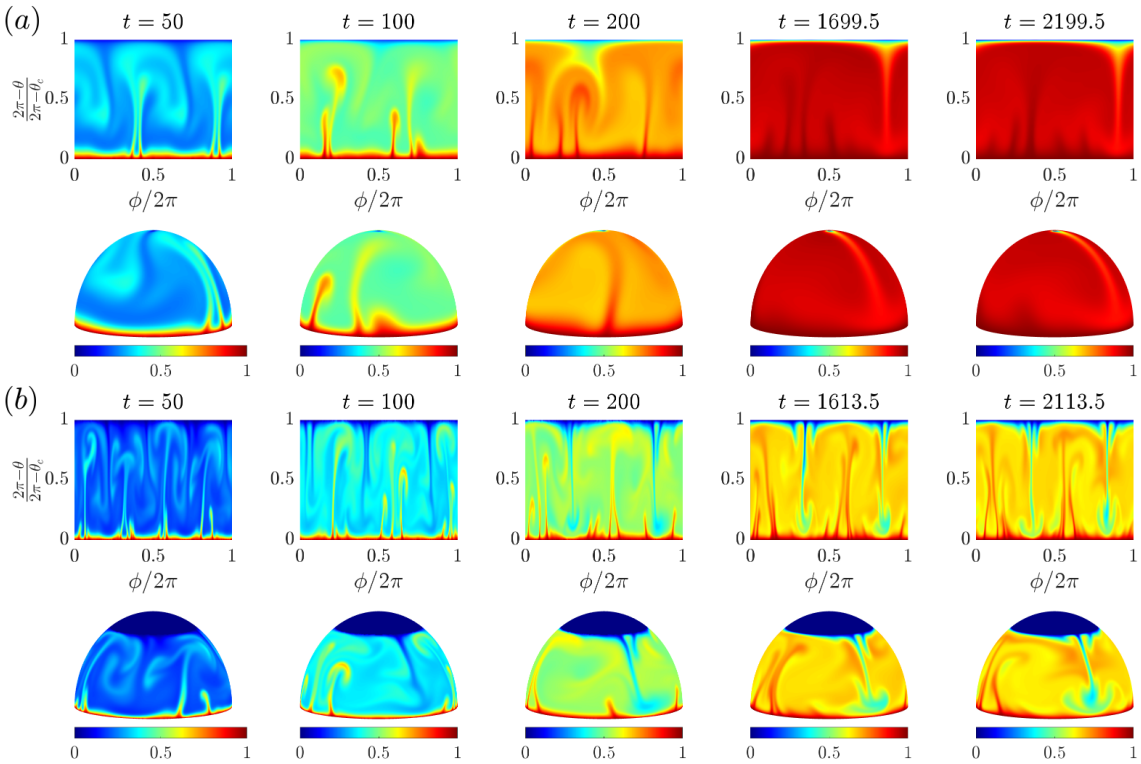

Figure 6: Evolution in time of the temperature fields. Top row: non-dimensional plan of the convective zone Ω_1 and bottom row: cavalier perspective of the entire bubble. (a) SR regime and (b) AR regime.

To validate the explanations above, Figure 6 (a) and (b) show two time series of temperature field snapshots for $A = 50.01$, $\text{Ra} = 1.12 \times 10^6$ (SR), and $A = 1.82$, $\text{Ra} = 2.89 \times 10^6$ (AR), respectively.

In Figure 6 (a), thermal convection is highly active at the beginning of DNS ($t = 50$ and $t = 100$). More hot plumes than cold plumes are observed, suggesting that thermal convection near $\mathcal{L}_h$ is notably stronger than near $\mathcal{L}_c$. This phenomenon implies that the heat transported into the convection zone exceeds the heat conveyed out. Therefore, for $t = 200$, an noticeable

rise of T_{Ω_1} is observed, driven by the heat accumulation within the convection zone. In addition, thermal convection weakens near the hot boundary $\mathcal{L}_h$. The snapshots for $t = 1699.5$ and $t = 2199.5$ clearly demonstrate that T_{Ω_1} reaches very high level. At this stage, thermal convection becomes inactive not only near $\mathcal{L}_h$ but also throughout the entire convection zone. Meanwhile, the temperature gradient near $\mathcal{L}_c$ is extremely steep, maximizing the heat transport out. However, owing to the weak gravitational component along the polar direction, even such a strong temperature gradient is insufficient to promote vigorous thermal convection.

In contrast, Figure 6 (b) shows a different pattern in the AR. The heat accumulation ceases at a relative low level as shown in the snapshot of $t = 1613.5$ and $t = 2113.5$. Unlike the SR, the balance between H_{out} and H_{in} is achieved with moderate T_{Ω_1}. Thermal convection remains consistently active throughout the entire convection zone.

4 Conclusion

In this work, we introduced the frozen top bubble model, which is a novel RBC configuration. It is derived from the half soap bubble model described in previous studies. One of the key features of the frozen top bubble model is the asymmetry between the hot and cold boundaries: the hot boundary is consistently longer than the cold boundary. This asymmetry is quantified by the non-dimensional parameter A, defined as the ratio of the length of the hot boundary to that of the cold boundary. Two distinct regimes were identified based on the value of A: the conditionally stable Stagnant Regime (SR) and the unconditionally stable Active Regime (AR). The convection zone Ω_1 is in the Stagnant Regime when the input parameter A is large, as the effect of the asymmetry is dominant. In this regime, the stability of the system diminishes as Ra increases. The strong asymmetry leads to a high-level accumulation of heat, severely constraining thermal convection. When A is close to 1, the model is in the Active Regime, where thermal convection is dominant. Convection is sustained, and the system remains stable regardless of the value of Ra. The heat accumulation is minimal, allowing active thermal convection.

The frozen top bubble model provides valuable insights into the effects of boundary asymmetry on thermal convection. The transition between the SR and the AR highlights the critical role of asymmetry in influencing stability, heat transport, and convection dynamics. This model serves as a robust framework for further exploration of asymmetric convection systems.

5 Acknowledgements

This work was co-funded by AAPG2022 research project LiFT (French National Research Agency funding) and the National Natural Science Foundation of China grant numbers 11872187 and 12072125. The authors thank MCIA (Mésocentre de Calcul Intensif Aquitain) of the University of Bordeaux for providing computing resources and technical support.

References

[1] D. Lohse and O. Shishkina. Ultimate turbulent thermal convection. *Physics Today*, 76(11):26–32, 11 2023.

[2] Y-C. Xie, L. Zhang, G. Ding, X. Chen, H. Xi, and K-Q. Xia. Progress in turbulent thermal convection in the past decade and outlook. 力学进展, 53(1):1–47, 2023.

[3] H. Kellay and W. Goldburg. Two-dimensional turbulence: a review of some recent experiments. *Reports on Progress in Physics*, 65(5):845, 2002.

[4] H. Kellay. Hydrodynamics experiments with soap films and soap bubbles: A short review of recent experiments. *Physics of fluids*, 29(11), 2017.

[5] F. Seychelles, Y. Amarouchene, M. Bessafi, and H. Kellay. Thermal convection and emergence of isolated vortices in soap bubbles. *Physical review letters*, 100(14):144501, 2008.

[6] T. Meuel, Y-L. Xiong, P. Fischer, C-H. Bruneau, M. Bessafi, and H. Kellay. Intensity of vortices: from soap bubbles to hurricanes. *Scientific reports*, 3(1):3455, 2013.

[7] T. Meuel, G. Prado, F. Seychelles, M. Bessafi, and H. Kellay. Hurricane track forecast cones from fluctuations. *Scientific reports*, 2(1):446, 2012.

[8] Y-L. Xiong, P. Fischer, and C-H. Bruneau. Numerical simulations of two-dimensional turbulent thermal convection on the surface of a soap bubble. *Proc ICCFD*, 7:3703, 2012.

[9] C-H. Bruneau, P. Fischer, Y-L. Xiong, and H. Kellay. Numerical simulations of thermal convection on a hemisphere. *Physical Review Fluids*, 3(4):043502, 2018.

[10] X-Q. He, A. Bragg, Y-L. Xiong, and P. Fischer. Turbulence and heat transfer on a rotating, heated half soap bubble. *Journal of Fluid Mechanics*, 924:A19, 2021.

[11] T. Meuel, M. Coudert, P. Fischer, C-H. Bruneau, and H. Kellay. Effects of rotation on temperature fluctuations in turbulent thermal convection on a hemisphere. *Scientific Reports*, 8(1):16513, 2018.

[12] X-Q. He, Y-L. Xiong, A. Bragg, P. Fischer, and H. Kellay. The effect of tilt on turbulent thermal convection for a heated soap bubble. *Physics of Fluids*, 34(10), 2022.

[13] F. Seychelles, F. Ingremeau, C. Pradère, and H. Kellay. From intermittent to non-intermittent behavior in two-dimensional thermal convection in a soap bubble. *Physical review letters*, 105(26):264502, 2010.

[14] P. Angot, C-H. Bruneau, and P Fabrie. A penalization method to take into account obstacles in incompressible viscous flows. *Numer. Math.*, 81:497, 1999.

[15] B-Y-C. Cheng, L. Zhang, K-Q. Xia, and Y-C. Xie. Effects of asymmetric rough boundaries on turbulent rayleigh–bénard convection. *Journal of Fluid Mechanics*, 997:A72, 2024.

[16] J. Paret and P. Tabeling. Intermittency in the two-dimensional inverse cascade of energy: Experimental observations. *Physics of Fluids*, 10(12):3126–3136, 12 1998.